Supplementary information

A lamellar dense anode enabling high-energy, ultra-high-rate and durable sodium storage

Jianhai Pan[1,#], Zhefei Sun[1,#], Jiaming Zhang[1,#], Peng Ouyang[2], Huiping Yang[4], Xiaoyu Wu[1], Boyang Shi[1], Yurui Xing[5], Longbang Di[6], Shenghui Zhou[1], Xingqi Chen[1], Wen Ren[7], Lei Gao[6], Hongti Zhang[5], Hui Yang[2,*], Li Zhang[4], Zaiping Guo[3,*], Qiaobao Zhang[1,*]

[1] State Key Laboratory of Physical Chemistry of Solid Surfaces, College of Materials, Xiamen University, Xiamen 361005, China

[2] State Key Laboratory of Material Processing and Die & Mould Technology, Department of Mechanics, School of Aerospace Engineering, Huazhong University of Science and Technology, Wuhan, Hubei 430074, China

[3] Department of Materials Science and Engineering, City University of Hong Kong, Hong Kong, P. R. China

[4] State Key Laboratory of Physical Chemistry of Solid Surfaces, College of Chemistry and Chemical Engineering, Xiamen 361005, Fujian, China.

[5] ShanghaiTech University, School of Physical Science and Technology, 393 Middle Huaxia Road, Pudong New District, China, 201210

[6] School of Advanced Materials, Shenzhen Graduate School, Peking University, Shenzhen, 518055, China.

[7] School of Chemistry and Chemical Engineering, Shanghai Jiao Tong University, Shanghai 200240, China

[#] These authors contribute equally to this manuscript

* Correspondence to: huiyang2017@hust.edu.cn (H. Yang); zaipiguo@cityu.edu.hk (Z. Guo); zhangqiaobao@xmu.edu.cn (Q. Zhang)

This PDF file includes:

Supplementary Text
Figs. S1 to S32
Tables S1 to S3
Reference

Other Supplementary Material for this manuscript includes the following:

Movies 1 to 8

Supplementary Text

Materials and methods

Preparation of Bi@C-MMS: First, 485 mg $Bi(NO_3)_3 \cdot 5H_2O$, 100 mg NaBr, 100 mg glucose, and 400 mg polyvinyl pyrrolidone (PVP) were dissolved in 50 ml ethylene glycol. The mixture was stirred for 10 minutes at room temperature to obtain a uniform solution. Then, 6% HNO_3 was added to the solution and stirred for another 30 min. After that, the mixed solution was transferred to a 100 mL PTFE lining and sealed with a stainless-steel shell for conducting a solvothermal reaction (150 ℃ for 12 h). After the reaction, the precursor was obtained by centrifuging the obtained mixture three times with deionized water and anhydrous alcohol. After drying, the precursor was then carbonized in a tube furnace at a temperature of 450 ℃ for 2 h with a heating rate of 2 °C min^{-1}.

Preparation of the C-MMS materials: In a typical preparation, 400 mg of Bi@C-MMS was stirred at room temperature in a 40% HNO_3 solution for 8 h to completely etch the metallic Bi. The resulting black powder was collected by suction filtration and drying at 120 ℃ for 10 h, yielding approximately 40 mg C-MMS.

Preparation of the Bi@C-SP: The synthesis conditions were adjusted by controlling the components of the reactants, Bi@C-SP was prepared under the same conditions as the synthesis of Bi@C-MMS but without HNO_3.

Materials characterization

The morphologies and structures of Bi@C-MMS were investigated through SEM (Zeiss SIGMA) and TEM (FEI Talos F200s). The 2D-ISXRD experiments were carried out at the BL02U2 beamline of the Shanghai Synchrotron Radiation Facility (SSRF), using a Pilatus 2M detector with an X-ray energy of 15.5 keV and a wavelength of 1.24 Å. XRD patterns were collected by a Bruker-ax 3s x-ray diffractometer (Cu Kα1 source, λ = 1.5418 Å). In-situ XRD was conducted on a Bruker D8 (Bruker Company) with Cu Kα radiation operating at 40 kV and 250 mA. Raman spectra were recorded with a Thermo Fischer DXR. BET analysis was characterized by a Micromeritics ASAP 2460 analyzer. A TGA (Netzsch TG 209 F3 Tarsus) was used to determine the weight change of the sample in air from room temperature to 800 ℃. XPS was performed on a Thermo Scientific Nexsa spectrometer. Tap density and compaction density of the sample were measured by JZ-1 powder vibration density meter and PCD2000 powder compaction density tester, respectively. In-depth XPS was performed by Thermo Scientific K-Alpha Nexsa with a monochromatic Al Kα x-ray source with a beam size of 400 um and energy: 1486.6 eV, voltage: 15 kV, beam current: 15 mA, analyses scan mode: CAE. Charge compensation was achieved by the dual beam charge neutralization and the binding energy was corrected by setting the binding energy of the hydrocarbon C 1s feature to 284.8 eV. TOF-SIMS data were collected using a IONTOF M6 instrument (IONTOF GmbH) equipped with a Bi liquid metal ion gun and Ar sputter gun. The analysis beam for this study was generated by the liquid metal ion gun, specifically a 30 keV Bi source, utilizing a Bi^{3+} rastered over an area of 80 × 80 um^2. The target current was measured as 0.43 pA. A 1 kV 50 nA Ar source was employed to etch through the sample over a 500 × 500 um^2 area. Sputter depth was calibrated using a 100 nm thick SiO_2 standard film. The sputtering interval was 0.3 nm s^{-1}. Data processing was done with the Surface Lab software.

Electrochemical measurements

The working electrode is composed of Bi@C-MS, carbon nano tubes (CNTs), carboxymethyl cellulose sodium binder (97:1.2:1.8 in weight), and deionized water, along with a copper foil current collector. After drying at 80 °C for 12 h, the slurry-coated copper foil was cut into discs with a diameter of 12 mm. The

loading of active material on electrodes is 1.2 mg cm^{-2}. NVP powder, CNTs and polyvinylidene fluoride (PVDF, 93.3:1.1:5.6 in weight) were evenly mixed in N-methylpyrrolidone (NMP), then coated on aluminum foil and dried under vacuum at 100 °C for 12 h to obtain NVP cathode. Assembling of CR2025-type half-cells was conducted in an argon-filled glovebox (MIKROUNA, China). In these half-cells, metallic sodium serves as the counter electrode, Celgard 2325 and Whatman GF/F glass fiber were used as the separator, and 1.0 M $NaPF_6$ in 1,2-dimethoxyethane (DME, DodoChem) was applied as the electrolyte. Bi@C-MS//NVP full cells and pouch cells were assembled with a negative/positive (N/P) capacity ratio of 1.25 ~ 1.30. The electrochemical performance tests, CV and GITT tests at room temperature were conducted on a battery testing system (Neware, MIHW-200-160CH-B) and an electrochemical workstation (CHI 660E), respectively. The voltage ranges were set as 0.01-1.6 V (Bi@C-MMS anode), 2.7-3.8 V (NVP cathode), and 2.2-3.2 V (Bi@C-MMS//NVP full cells and pouch cells), respectively. In-situ and ex-situ EIS tests were performed at the PARSTAT 3000A-DX and Chenhua (Shanghai, China) electrochemical workstations, respectively.

In-situ TEM measurements

The dynamic sodiation/desodiation process was investigated using a FEI Talos F200s TEM equipped with a Nanofactory TEM holder. Bi@C-MMS attached to the Cu tip serves as the working electrode. The Na metal was positioned at the W tip, serving as the counter electrode. The naturally formed Na_2O layer on the surface of the Na metal acted as the solid electrolyte. A bias voltage of 3 V/-3 V was applied to the Na/Na_2O electrode to drive the sodiation and desodiation of Bi@C-MS.

In-situ SEM micro-mechanical measurements

The in situ quantitative compression tests were performed inside SEM (JEM-IT500 HRSEM, 10 kV) with a BrikerTM Hysitron PI88 Picoindenter. Bi@C-MMS samples were attached to a 5 × 5 mm^2 silicon wafer randomly. Subsequently, the silicon substrate was installed on the specimen stage of PI88 Picoindenter. By monitoring the uniaxial compression tests and recording the videos in real time, the load-displacement curves can be exported. The compression tests were performed under pressure control with a load rate set at 5 nm s^{-1}.

Chemo-mechanical simulation methods

To elucidate the underlying mechanisms of Bi sodiation, we implemented chemo-mechanical simulation in ABAQUS based on our previous model to capture the interrelated evolution of phase transformation, stress concentration, and morphology during Na insertion [1,2]. A cake-like Bi@C-MMS model and a spherical Bi@C-SP model were constructed according to experiment specimens, with Na ions inserted from the outer boundary. Both models share the characteristic diameter of 725nm, and the thickness of the cake-shaped model is 225nm. For Bi@C-MMS, anisotropic expansion was applied, with expansion coefficient of 0.11 along the thickness direction and 0.03 in plane, corresponding to the experimentally measured expansion of 15% and 5% respectively. The Bi@C-SP was assumed to undergo isotropic expansion with uniform coefficient of 0.11. All other material properties used in the simulation were specified based on experimental measurements. For the sodiation-induced damage of the specimens, the cross sections of Bi@C-MMS and Bi@C-SP were considered, with cohesive interfaces constructed between carbon interlayers in Bi@C-MMS and along the boundaries of Bi/C nanosheets in Bi@C-SP [3,4].

SRCT measurements

SRCT imaging was collected at the beamline BL18B, Shanghai Synchrotron Radiation Facility (SSRF) to

analyze the 3D morphology of regions of interest within the battery by reconstructing the particles which before and after cycling. The nano tomography dataset imaging dataset was collected by 8 keV X-rays using 180 projections over a 180°angular range, and the resolution of this TXM has been quantified to a 3D resolution of less than 65 nm. The data were reconstructed in 3D using the Adu Recon software. The 3D visualization and data analysis were performed using the commercial software package Avizo (Thermo Fisher Scientific, Waltham, MA).

Figures

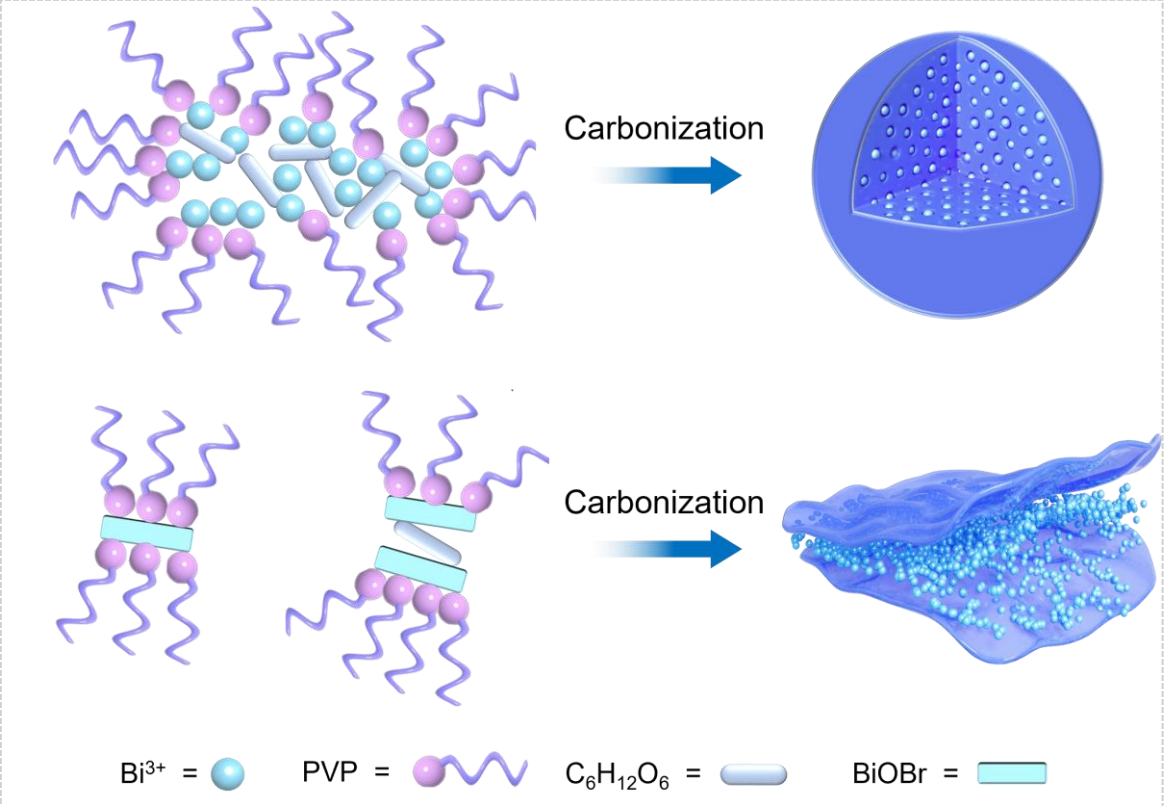

Fig. S1. PVP's disordered adsorption of Bi^{3+} and its specific adsorption of layered BiOBr. PVP molecules are strongly pinned to specific crystal planes of BiOBr through selective adsorption, significantly reducing the surface energy of these planes and inhibiting their growth. Meanwhile, the unadsorbed lateral surfaces maintain rapid growth rates. This anisotropic growth kinetics, induced by selective adsorption, drives BiOBr crystals to preferentially expand along a two-dimensional direction into nanosheets. The subsequent carbonization process then solidifies this template morphology. It is noteworthy that in the absence of strong acids, Br^- triggers explosive nucleation of BiOBr. PVP rapidly and indiscriminately envelops numerous minute crystalline nuclei in an isotropic manner, leading to their agglomeration into spherical structures (formation of Bi@C-SP precursor). Conversely, within the strongly acidic environment created by nitric acid, the stable carboxylic acid coordination complex formed between Bi^{3+} and oxidized glucose acts as a 'controlled-release source'. This enables BiOBr to precipitate slowly and in a controlled manner. During this phase, PVP possesses sufficient time to perform crystal-face-specific adsorption, preferentially inhibiting the growth of specific crystal faces. This strategically guides the crystals towards anisotropic two-dimensional expansion, ultimately yielding a layered structure (formation of Bi@C-MMS precursor).

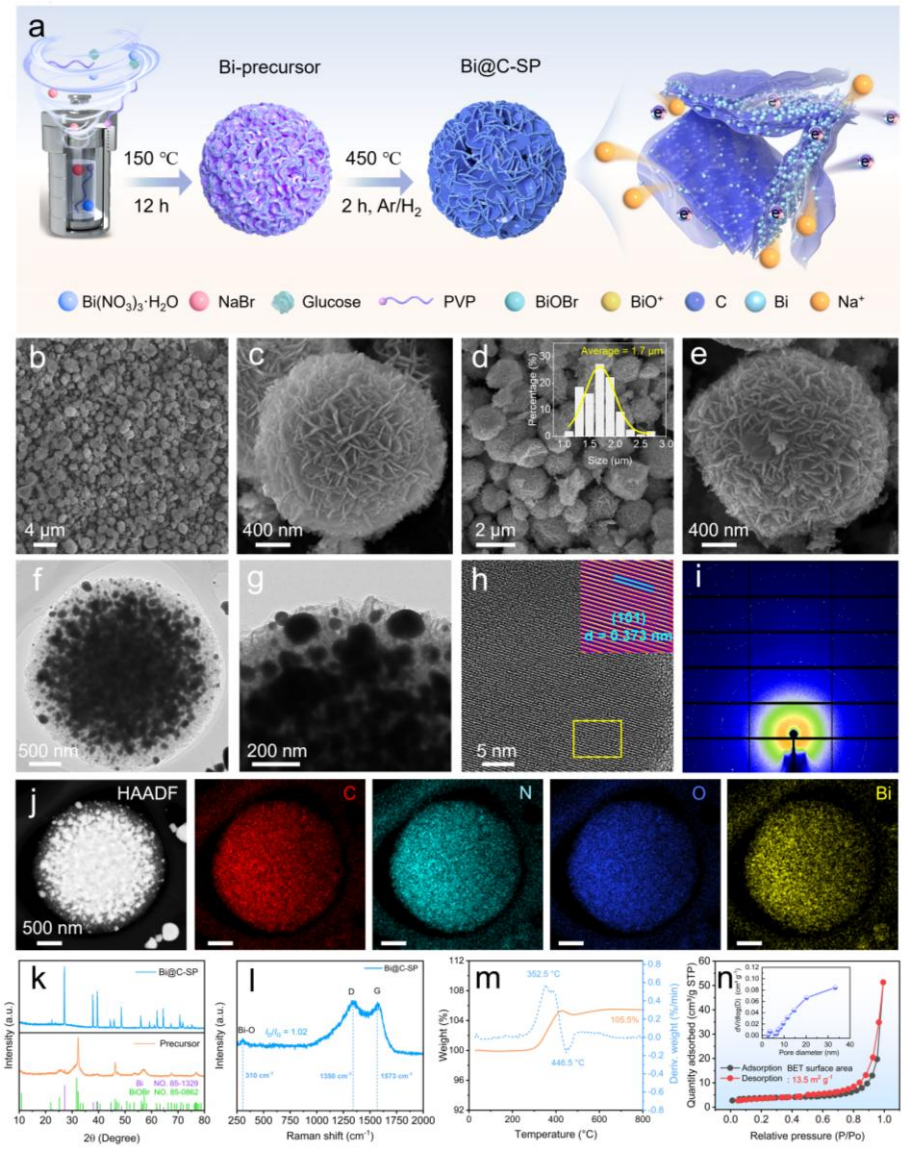

Fig. S2. a Schematic illustration of the synthesis process of Bi@C-SP composite. **b-e** SEM images of the precursor and Bi@C-SP. **f-h** TEM and HR-TEM images of Bi@C-SP **i** 2D-GISXRD patterns for Bi@C-SP. **j** Elemental mappings of C, N, O, Bi. **k** XRD, **l** Raman pattern, **m** TGA and DTG curves, **n** N_2 adsorption/desorption isotherms and pore-size distribution (inset) of Bi@C-SP. The following oxidation equation occurs for the Bi@C-SP during the TGA test:

$$C + O_2 \rightarrow CO_2$$

$$4Bi + 3O_2 \rightarrow 2Bi_2O_3$$

Based on the reaction above, during the TGA test, the carbon within Bi@C-MMS reacts with oxygen from the air at high temperatures, producing gaseous CO_2, while metallic bismuth reacts to form solid Bi_2O_3. The final product determined from the TGA curve is Bi_2O_3, accounting for a weight of 105.5%. Then, the content of bismuth (w_{Bi}) is calculated based on the stoichiometry in the following equation (M_{Bi} = 209 g mol^{-1}, M_{Bi2O3} = 466 g mol^{-1}):

$$\frac{4 \times 209}{w_{Bi}} = \frac{2 \times 466}{105.5\%}$$

By calculation, the mass percentage of bismuth in Bi@C-SP is approximately 94.6%, while the mass percentage of carbon is approximately 5.4%.

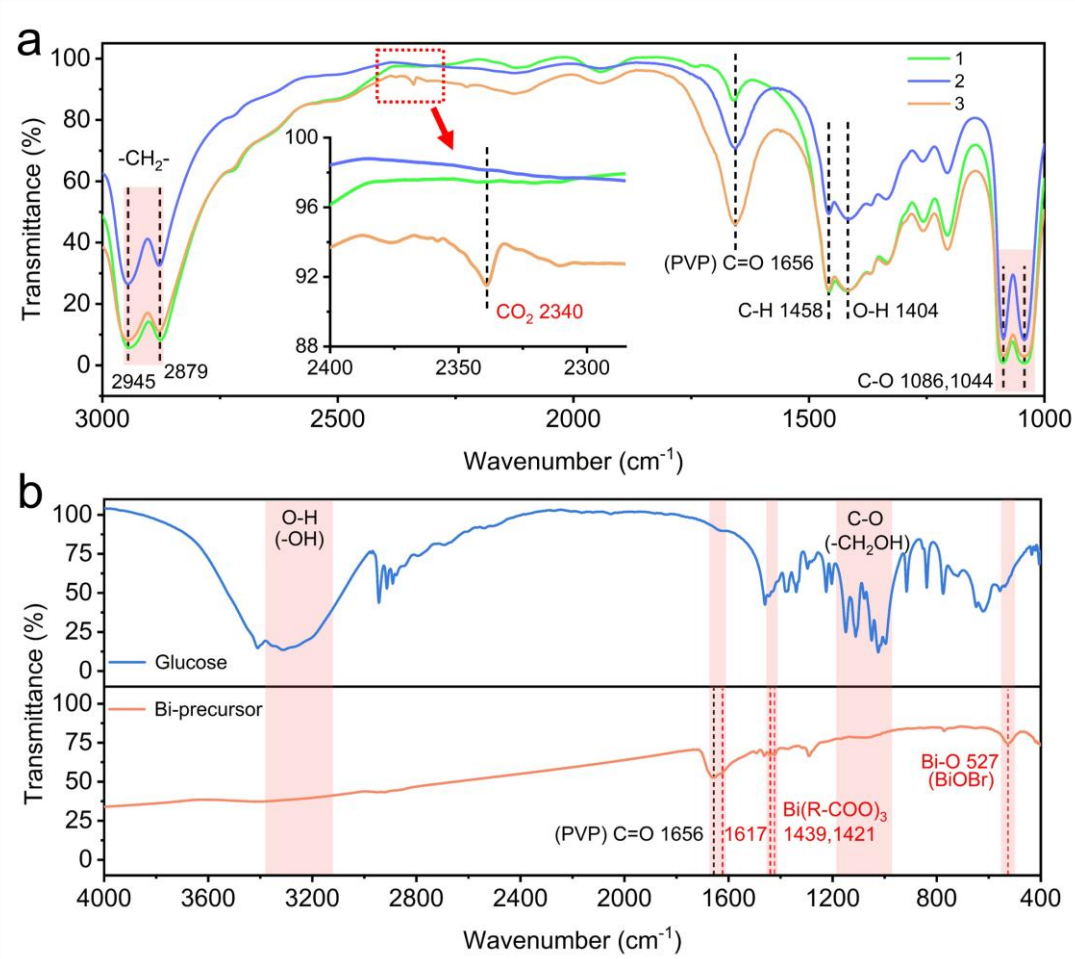

Fig. S3. a FTIR spectroscopy of the mixed solution obtained during the Bi@C-MMS synthesis process (1) without the addition of HNO_3, (2) with the addition of HNO_3, and (3) after heating the reaction mixture. **b** FTIR spectroscopy of glucose and the Bi@C-MMS precursor. The FTIR spectra of the three liquid samples in **Fig. S3a** are essentially identical, but upon heating, characteristic peaks for CO_2 emerge, resulting from the decomposition of free carboxylic acids. This demonstrates the presence of -COOH in the solution environment. **Fig. S3b** clearly demonstrates the complete conversion of glucose to glucaric acid, hence the absence of characteristic peaks for -OH and -CH_2OH groups in the Bi-precursor. The characteristic peaks at wavenumbers 527 cm^{-1}, 1421 cm^{-1}, 1439 cm^{-1}, and 1617 cm^{-1} confirm the presence of BiOBr and the coordination of the carboxyl group in malonic acid with Bi^{3+}.

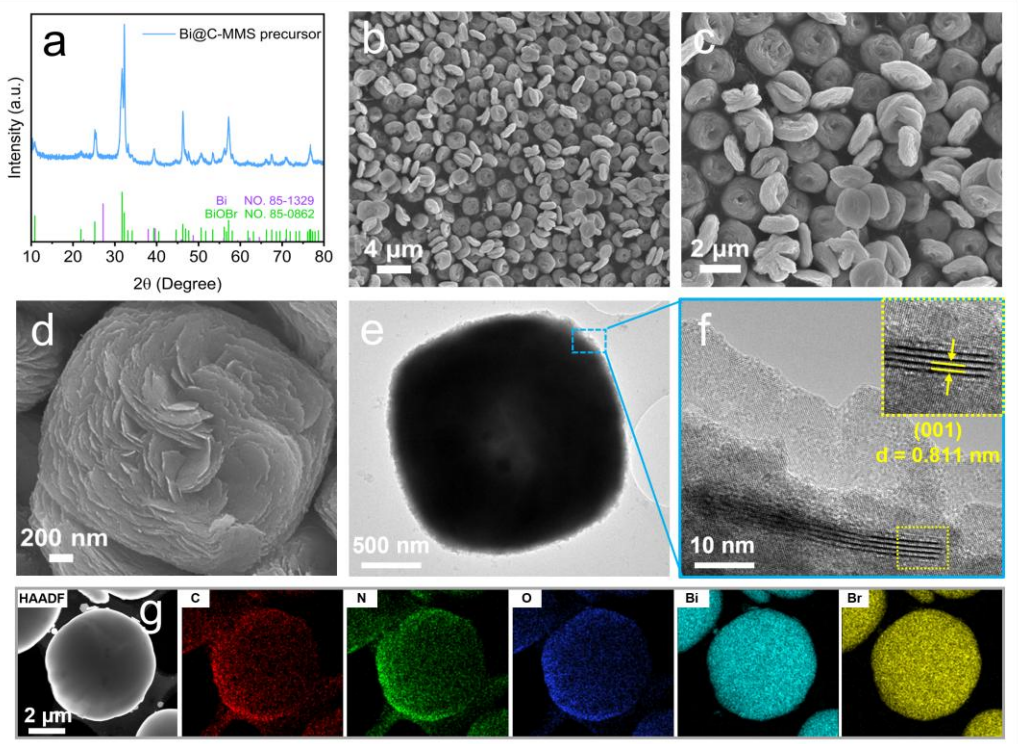

Fig. S4. a XRD spectrum, **b-d** SEM images. **e**, **f** TEM and HR-TEM images and (**g**) Elemental mappings of Bi@C-MMS precursor.

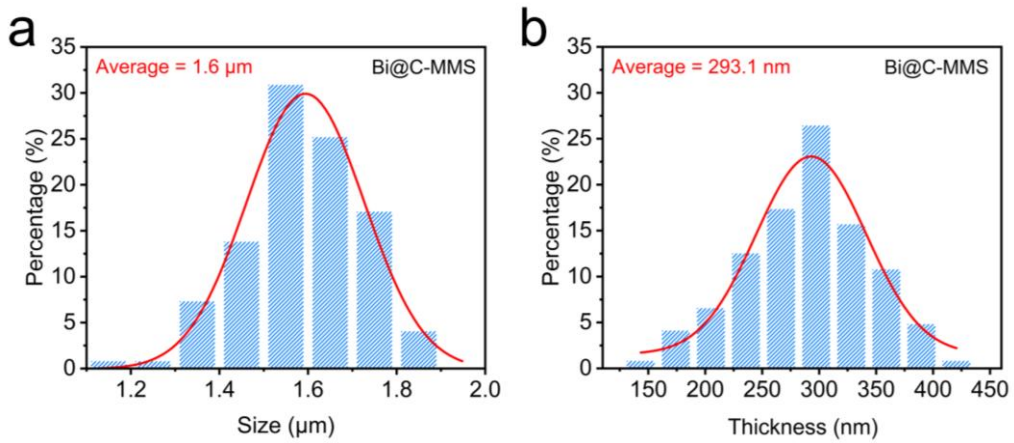

Fig. S5. Particle size distribution diagram of Bi@C-MMS and its thickness.

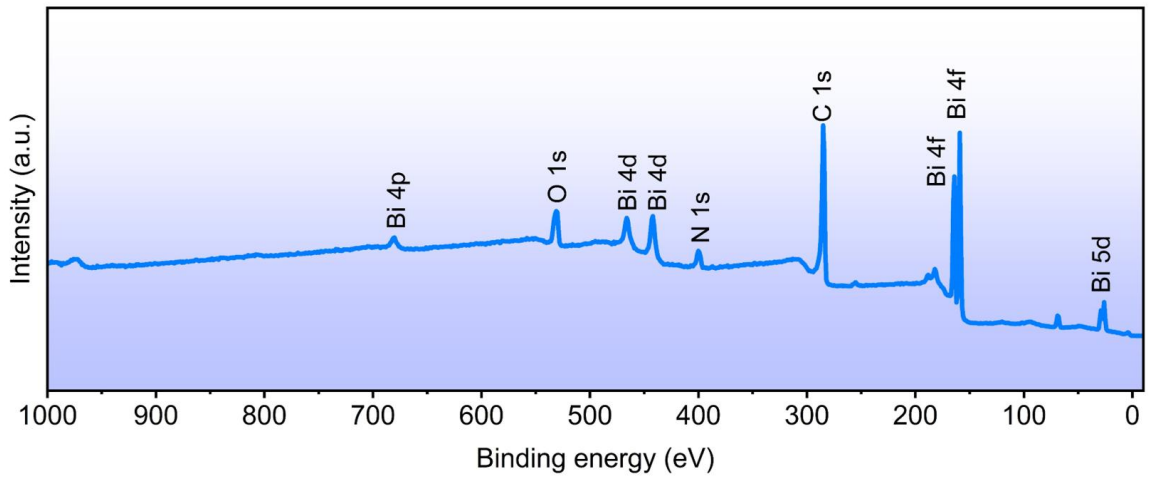

Fig. S6. XPS spectrum of Bi@C-MMS.

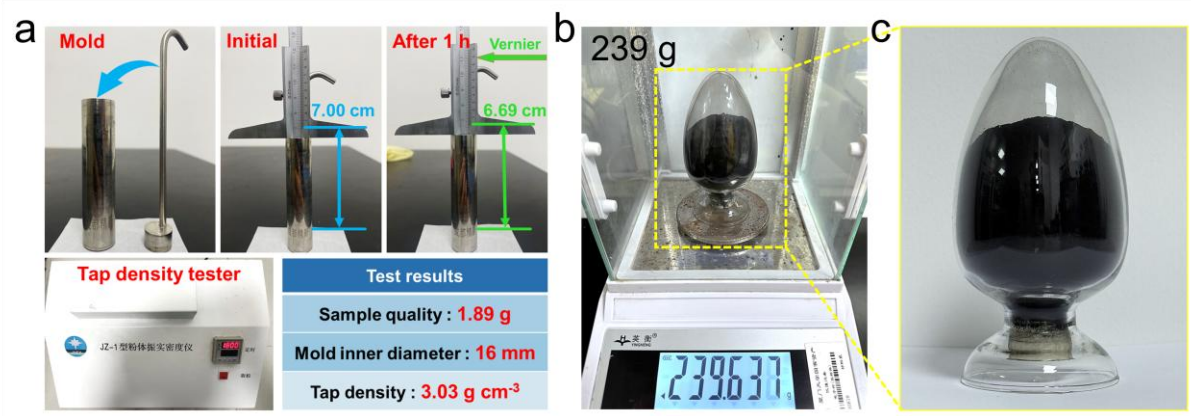

Fig. S7. **a** The tap density of Bi@C-MMS and (**b**, **c**) single-batch yield after amplification of reactants. In (**a**), the powder sample of Bi@C-MS, weighing 1.89 g, was placed in a cylindrical mold with a depth of 7.00 cm. Upon placing the sample and fully settle for 1 h, the measured depth inside the mold was 6.69 cm. The base area of the cylindrical mold is 2.01 cm^2. Assuming the tapped density of Bi@C-MMS is denoted by y, it can be calculated using the following equation:

$$y = \frac{1.89}{(7.00 - 6.69) \times 2.01}$$

It is calculated that $y = 3.03$, that is, the tap density of Bi@C-MMS is 3.03 g cm^{-3}.

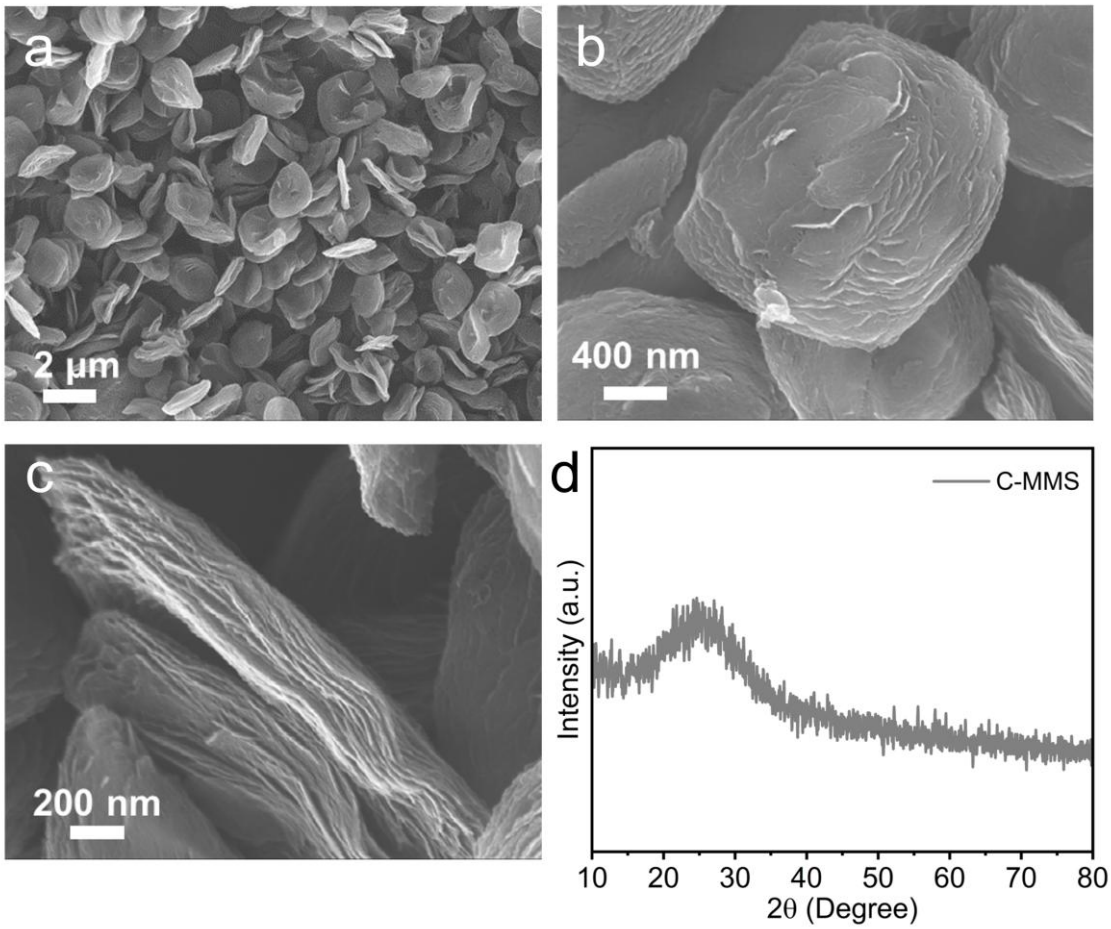

Fig. S8. a-c SEM images and (**d**) XRD spectrum of C-MMS.

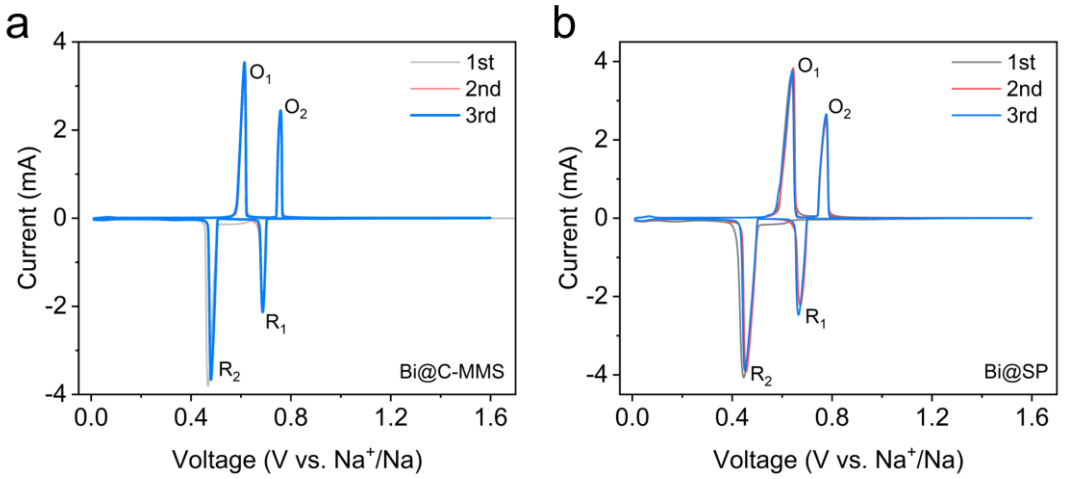

Fig. S9. CV curves of the first three cycles of (**a**) Bi@C-MMS and (**b**) Bi@C-SP at the scan rate of 0.2 mV s^{-1}.

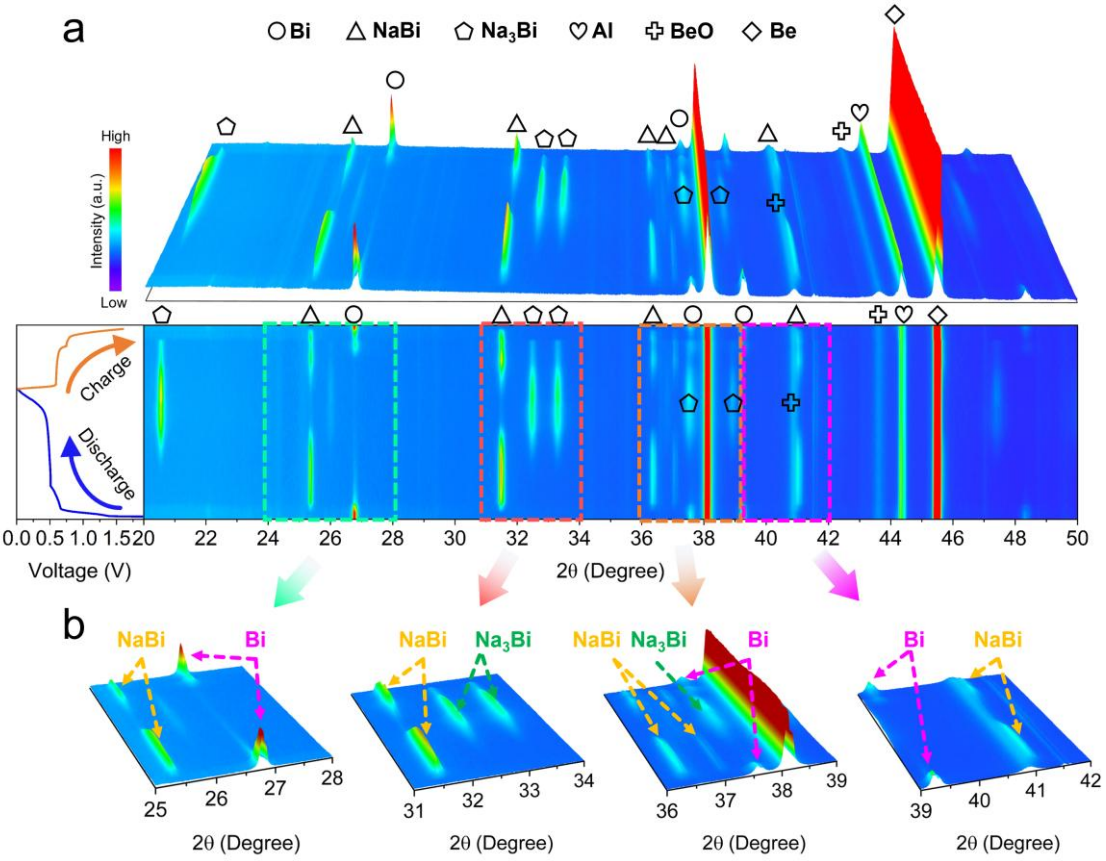

Fig. S10. In-situ XRD pattern of Bi@C-MMS during the first charge/discharge process at 0.1 A g^{-1}. **a** 3D and contour plot, and corresponding discharge/charge curves (the left), **b** Magnified detail from in situ XRD patterns in diffraction angle ranges of 25.0–28.0°, 31.0–34.0°, 36.0–39.0°, and39.0–42.0° corresponding to the marked rectangular regions, respectively.

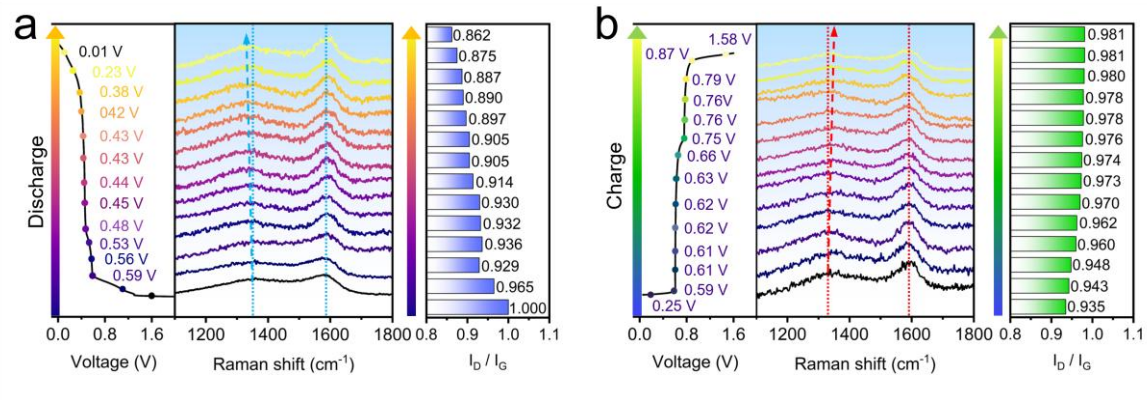

Fig. S11. In-situ Raman curves during the first cycle of Bi@C-MMS along with corresponding I_D/I_G values.

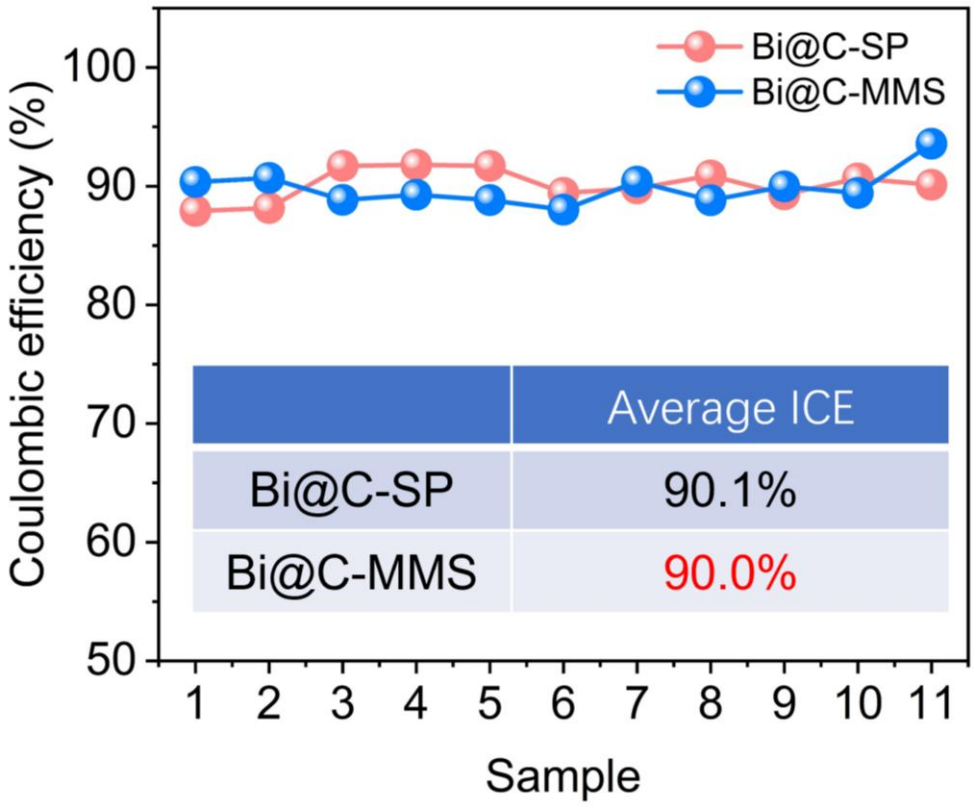

Fig. S12. Statistical Chart of ICE for Bi@C-MMS and Bi@C-SP.

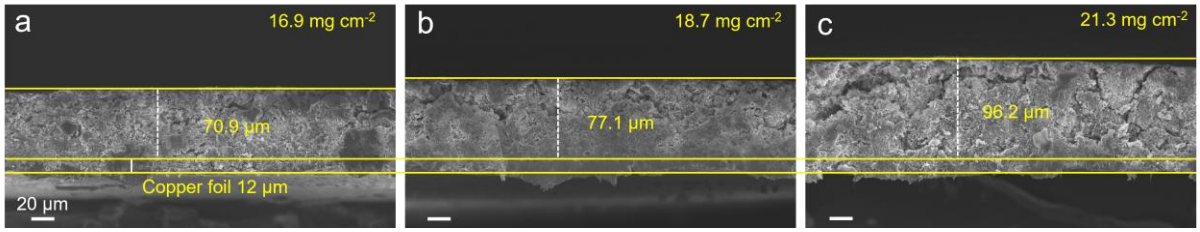

Fig. S13. Cross-sectional thickness of the electrode at different loading.

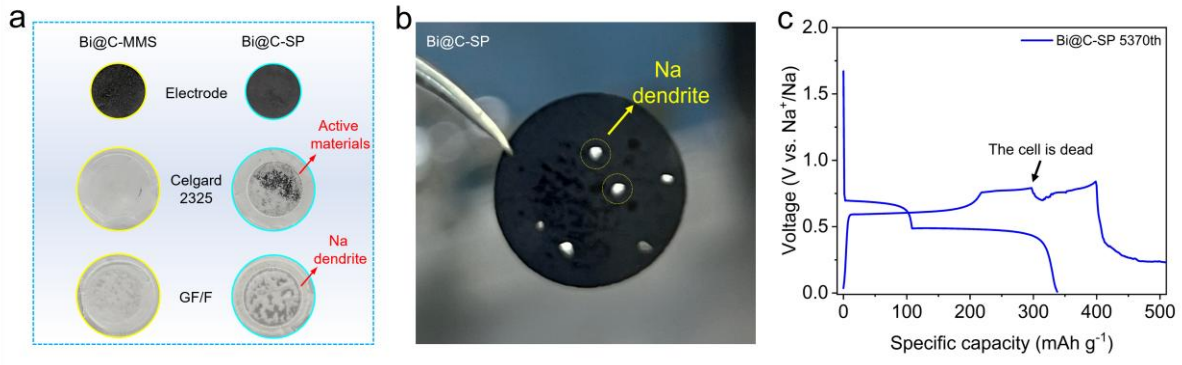

Fig. S14. a Residual active material and (**b**) sodium dendrites on the separator following Bi@C-SP battery failure, **c** along with the resulting voltage drop, do not occur in Bi@C-MMS batteries with the same number of cycles.

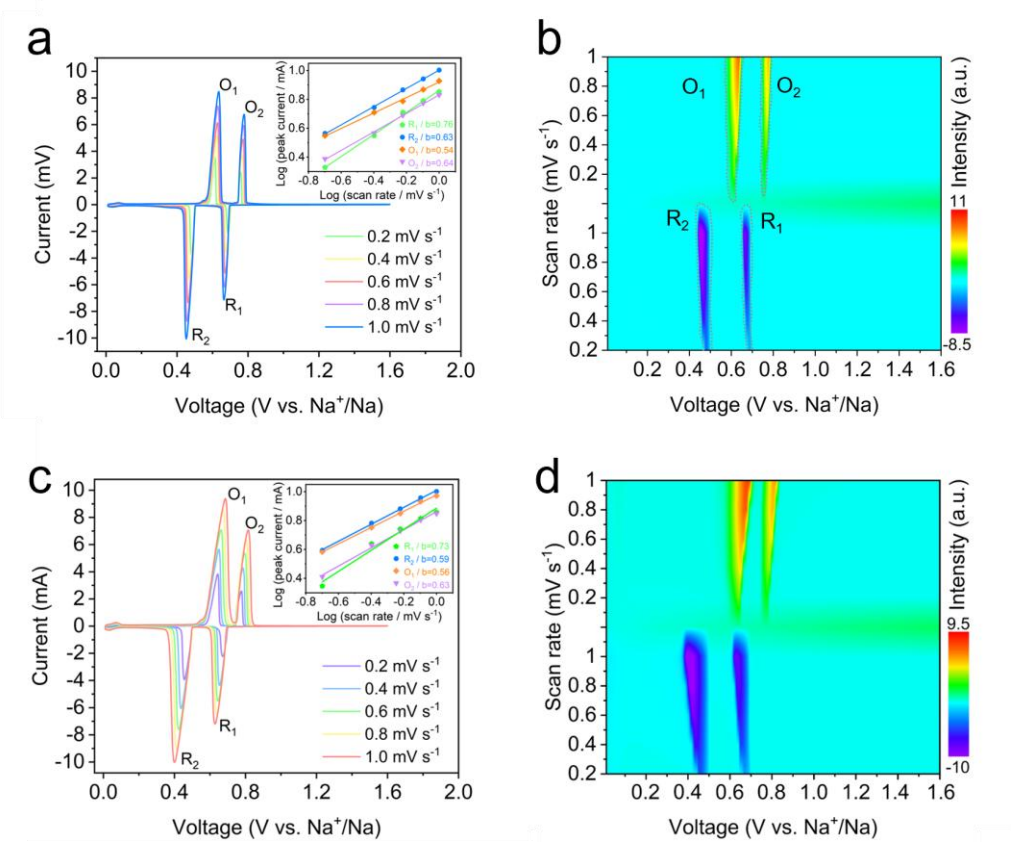

Fig. S15. a, **b** CV curves of Bi@C-MMS, (**c**, **d**) Bi@C-SP at different scan rates and corresponding contour map. The illustrations show the b values for various peak currents, typically employed to elucidate the sodium storage mechanism in materials via the following equation:

$$\log i = log\ a + b\ log\ v$$

where i denotes the peak current, a is a constant, and v represents the scan rate. They b values are consistently close to 0.5, indicating that the Na^+ storage process is dominated by diffusion behaviour; values closer to 1 suggest pseudocapacitive behaviour predominates.

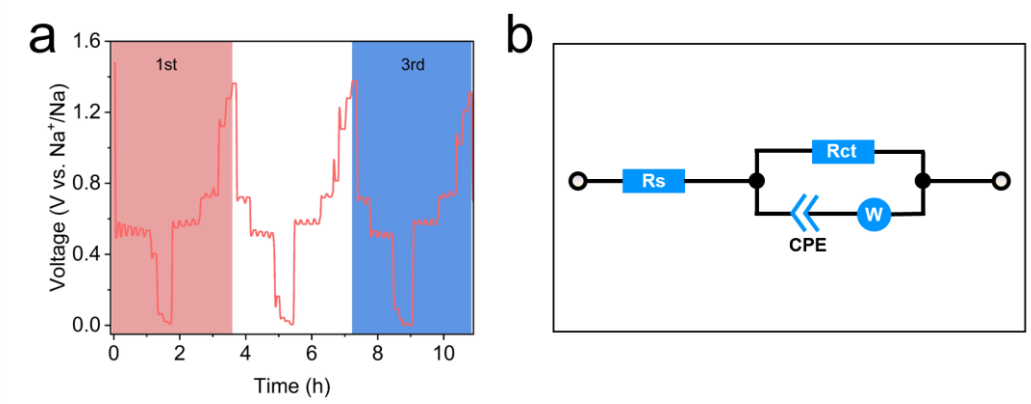

Fig. S16. a Voltage-time curve during Bi@C-MS in-situ EIS testing and corresponding and (**b**) equivalent circuit diagram.

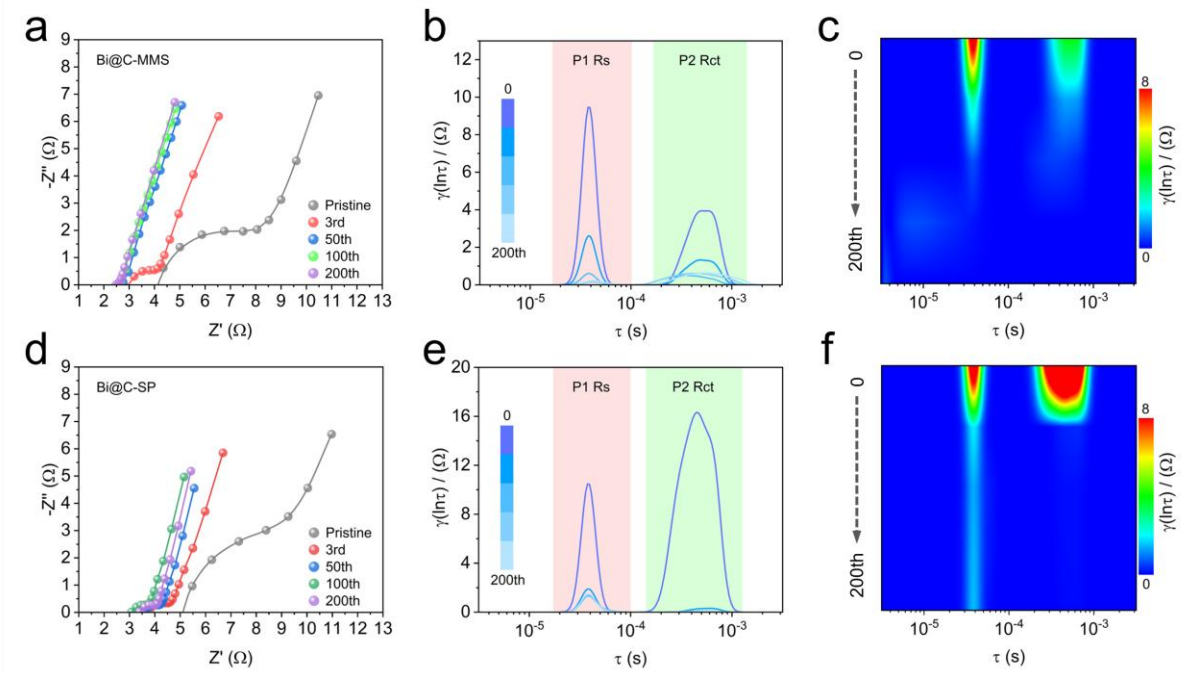

Fig. S17. a-c Ex-situ EIS plots and corresponding DRT curves and their contour maps of Bi@C-MMS and (**d-e**) Bi@C-SP.

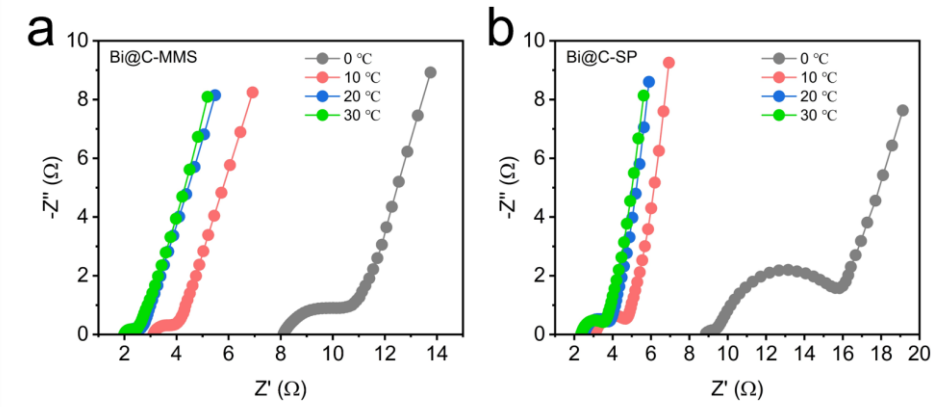

Fig. S18. a, **b** EIS plots of Bi@C-MMS and Bi@C-SP at various temperatures.

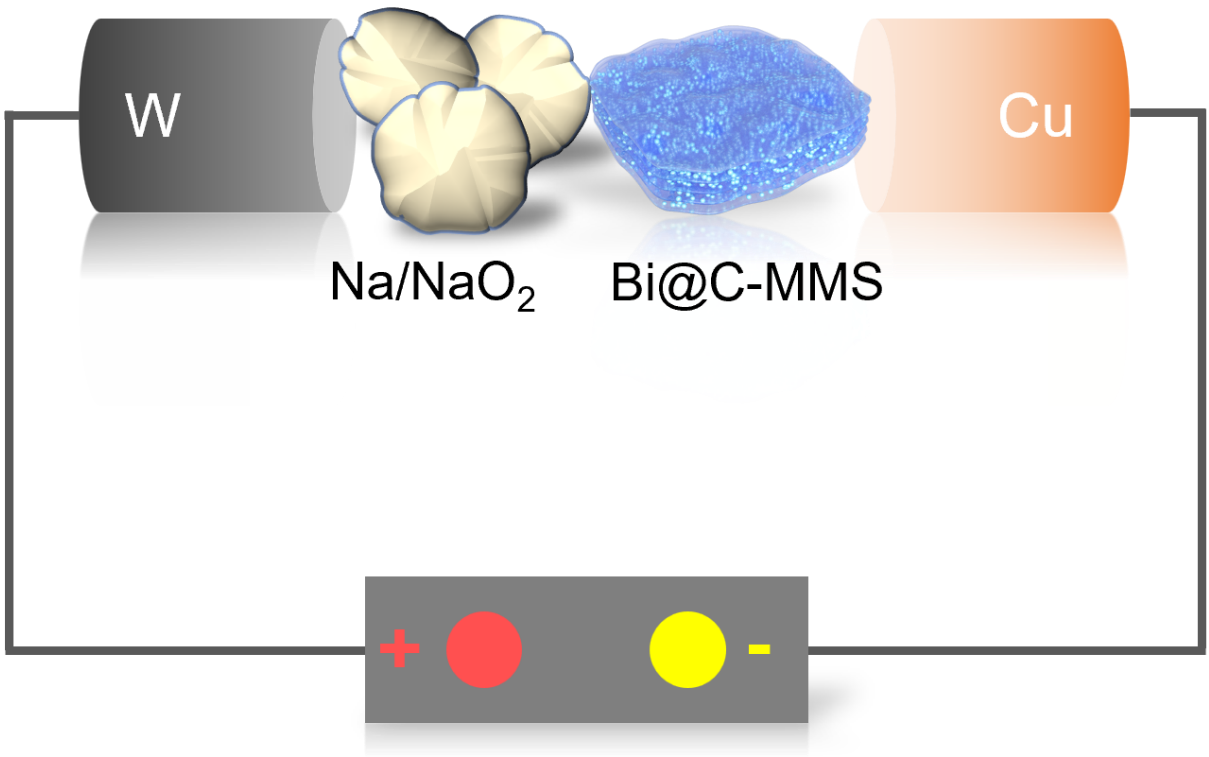

Fig. S19. In-situ TEM nanobattery device schematic.

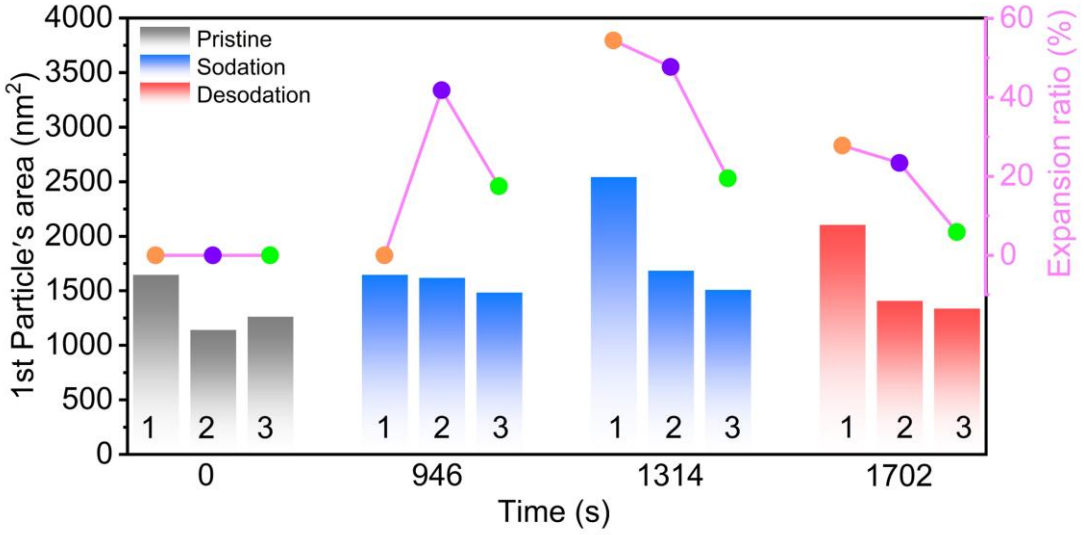

Fig. S20. The area variation process of bismuth nanoparticles at three positions within Bi@C-MMS during in-situ sodium insertion, along with the corresponding expansion ratios.

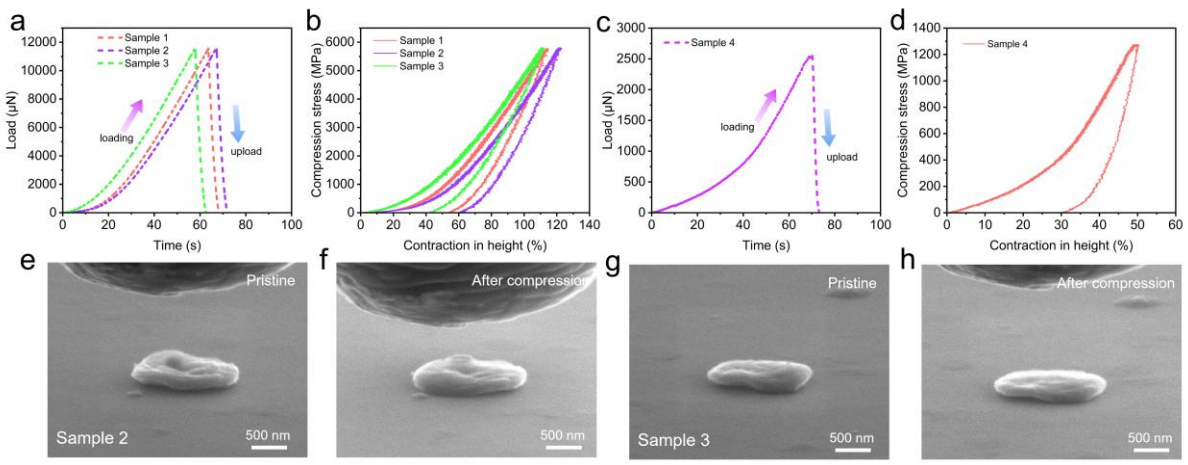

Fig. S21. Through in-situ SEM micro-mechanical testing, quantitative investigation of the mechanical properties of Bi@C-MMS particles in the thickness direction was conducted using the flat-plate compression method. Figures **(a-d)** present the load-time curves and stress-strain curves of Bi@C-MMS under varying loads, alongside **(e-h)** SEM images before and after compression. The yield stress (σ) and strain (ε) of the particles can be determined using the following formulas:

$$\sigma = \frac{F}{A}\ ;\ \varepsilon = \frac{L - L_0}{L_0}$$

In the equations, σ represents the yield stress, F denotes the load, A is the contact area (for simplification, it is approximately considered as the cross-sectional area of the particle), ε is the yield strain, and L and L_0 represent the height of the material after deformation and the initial height, respectively.

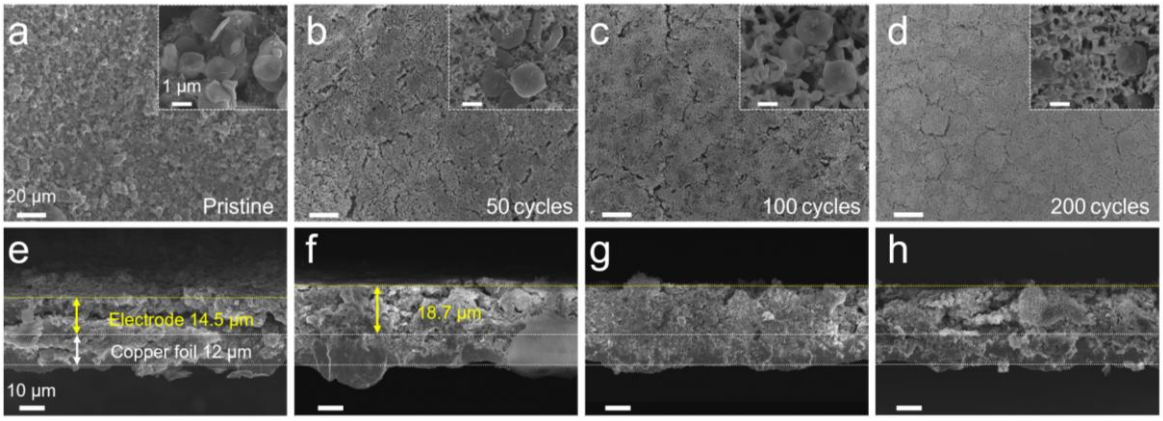

Fig. S22. SEM images of Bi@C-MMS electrode surface and thickness at different cycle numbers.

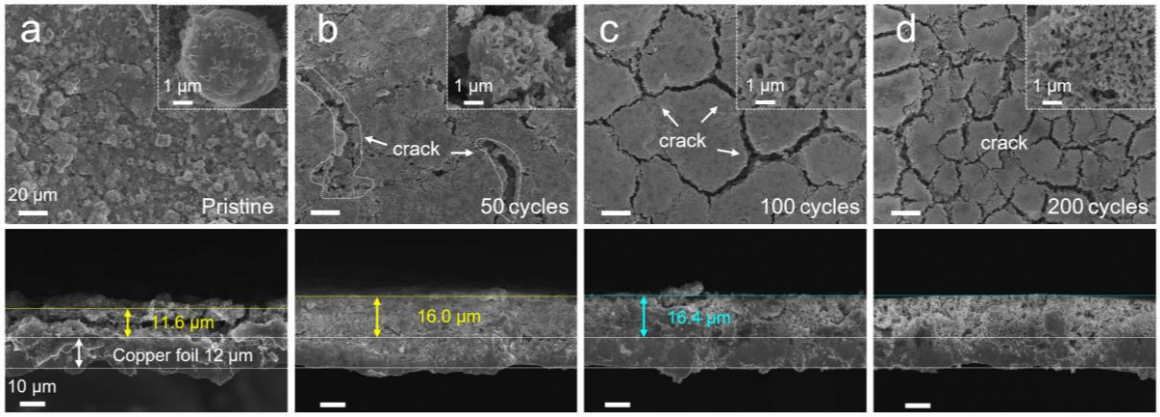

Fig. S23. SEM images of the surface and thickness of the Bi@C-SP electrode under different cycle numbers.

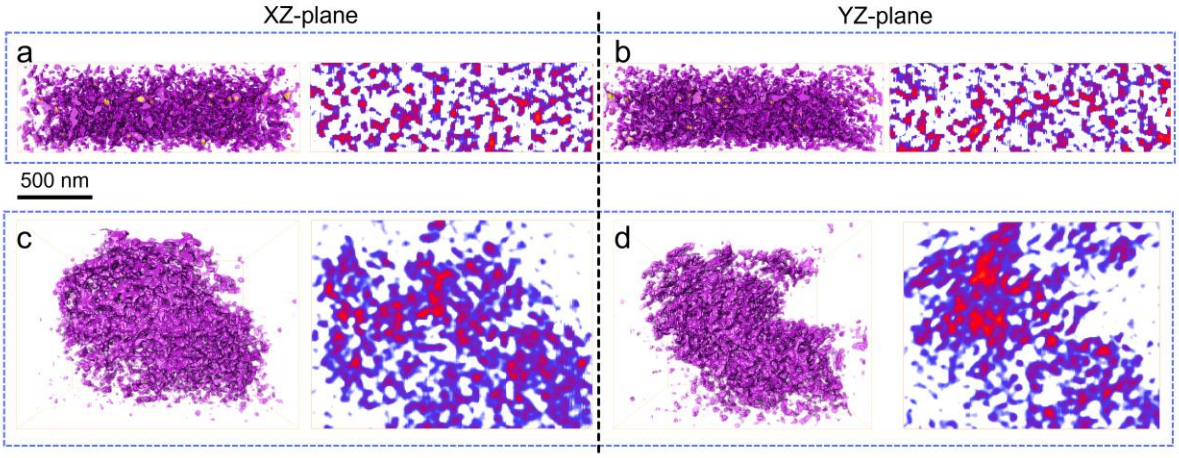

Fig. S24. 3D SRCT images of Bi@C-MMS from different perspectives at initial and 200 cycles, along with corresponding cross-sectional views.

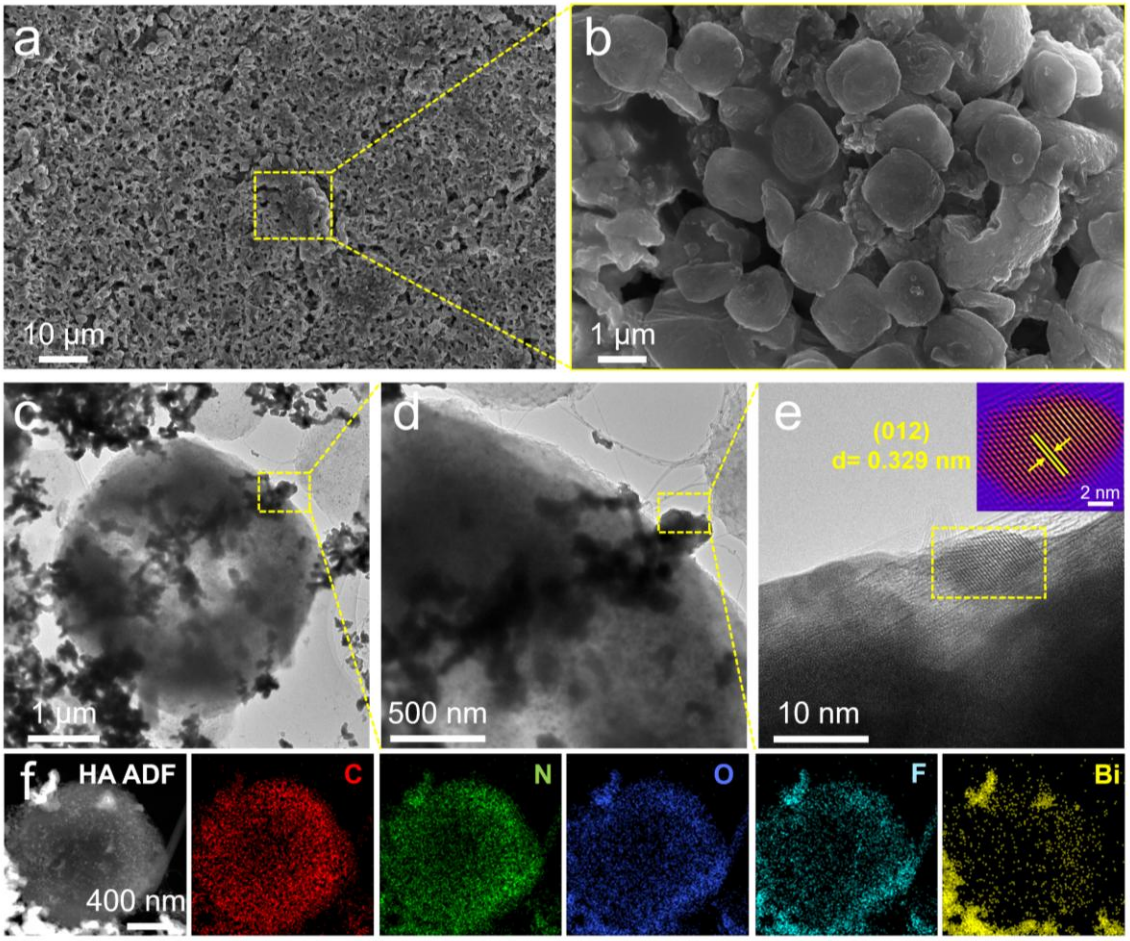

Fig. S25. a, **b** SEM images, **c**, **d** TEM images, **e** HR-TEM image and (**f**) elemental mapping images of the Bi@C-MMS electrode after 2000 cycles

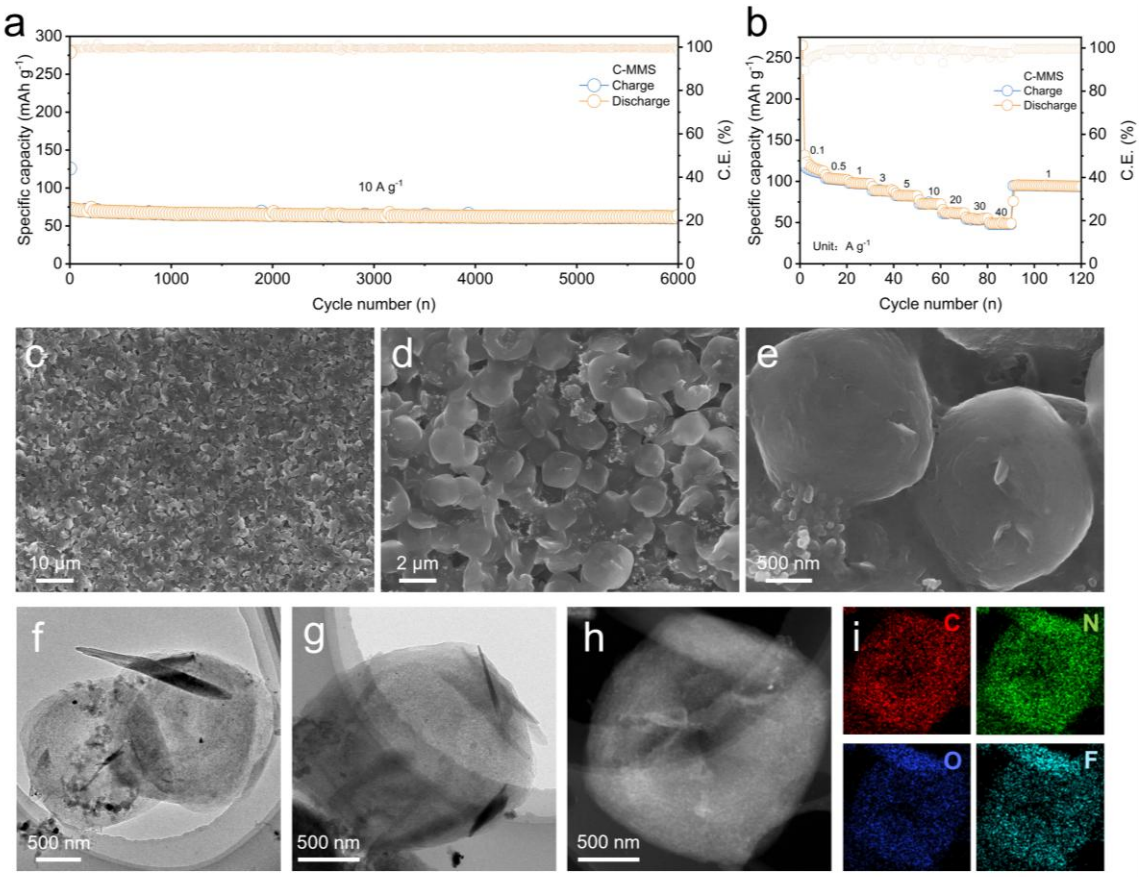

Fig. S26. a Long-cycle performance at 10 A g^{-1} and (**b**) rate capability of C-MMS, **c**-**e** along with the SEM images, **f**, **g** TEM images, **h** and elemental mapping images of the electrode after cycling.

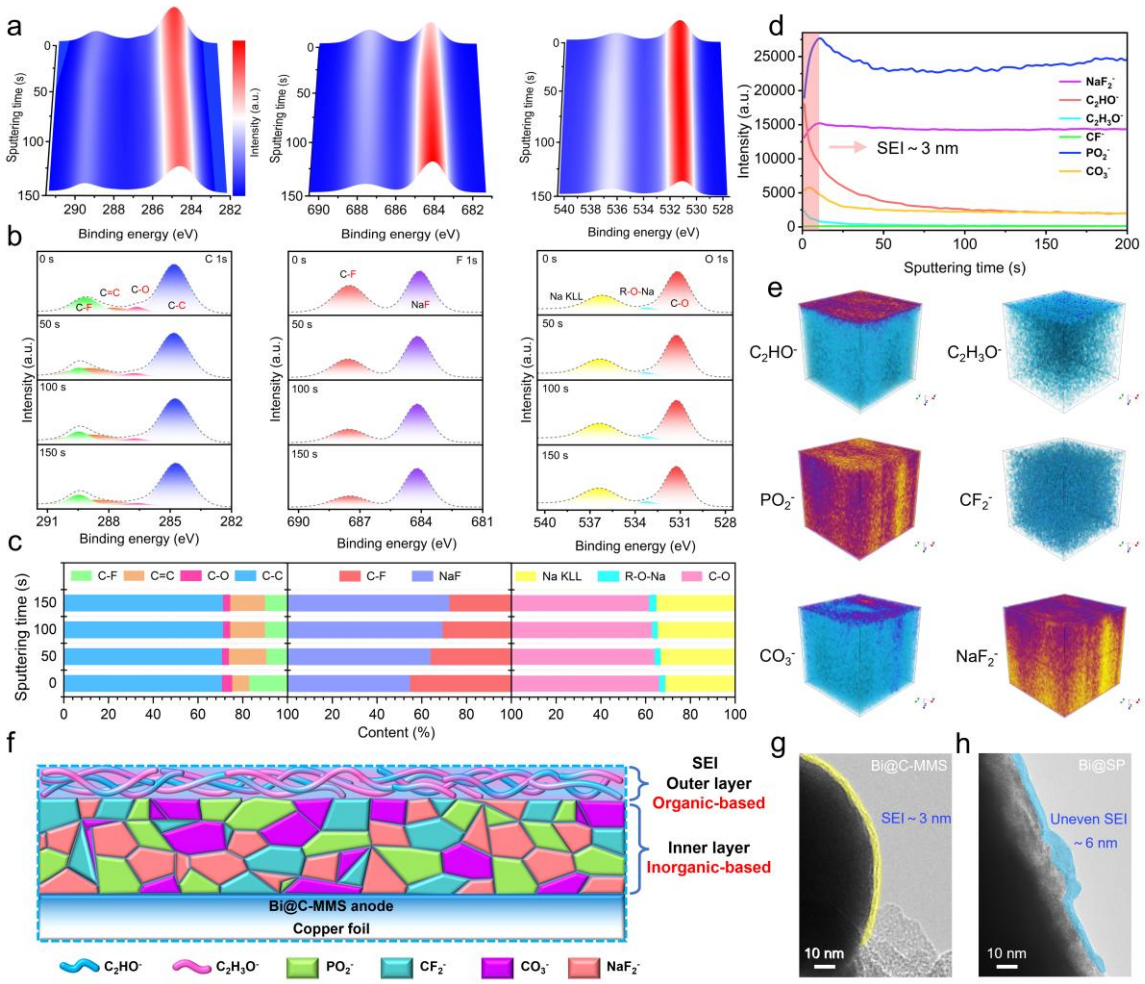

Fig. S27. SEI film analysis. **a**, **b** Evolution of C 1s, O 1s and F 1s and their fine spectra in Bi@C-MMS electrodes with sputtering time. **c** Relative content chart of each component in the XPS fine spectrum. **d** Depth distribution curves of various ions over sputtering time and (**e**) the corresponding 3D views of the sputtered surface and volume. **f** Schematic diagram of the composition and structure of gradient SEI film. **g**, **h** HR-TEM images of the surface SEI on Bi@C-MMS and Bi@C-SP electrodes after 200 cycles.

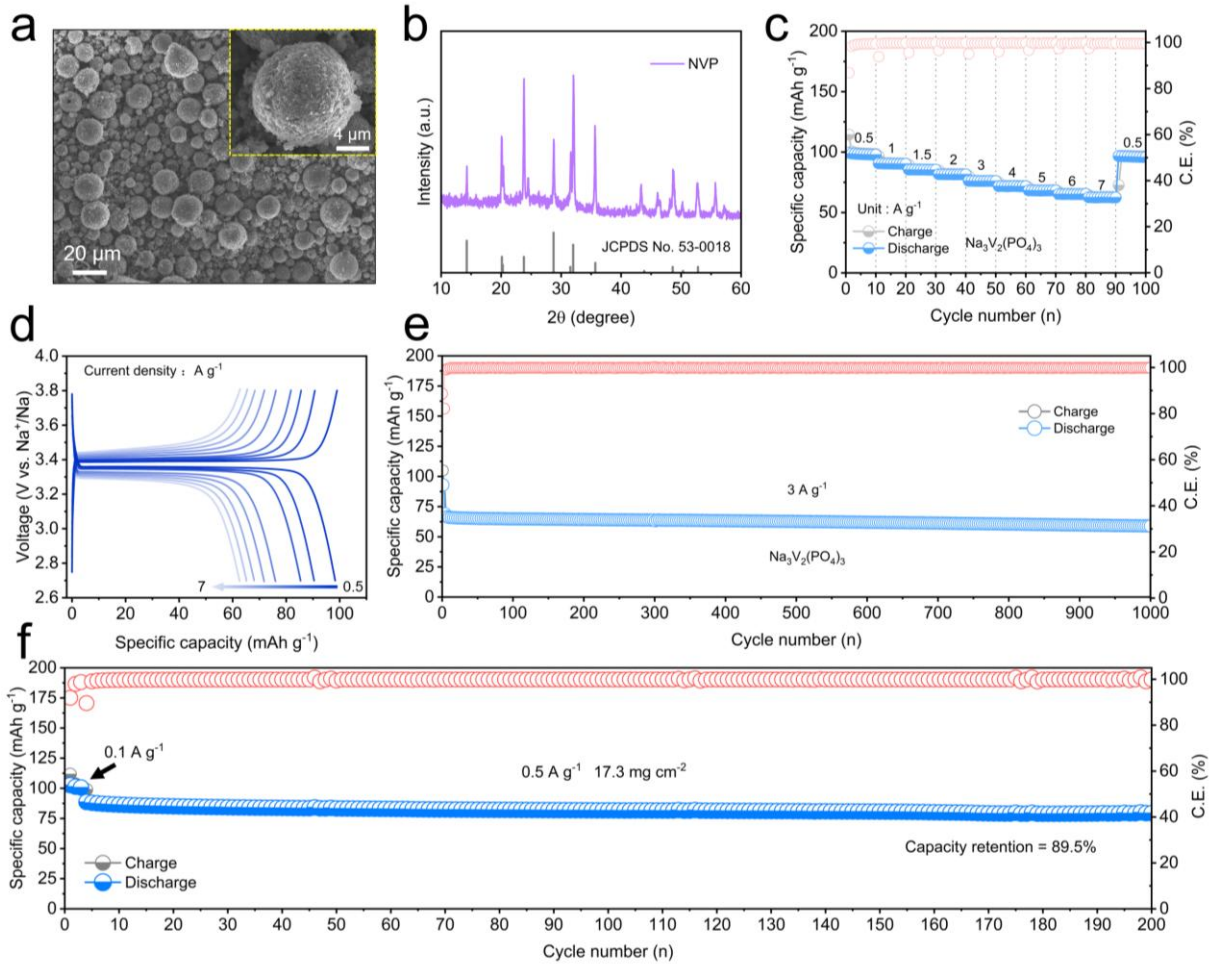

Fig. S28. a SEM image and (**b**) XRD pattern of NVP. **c**, **d** Rate performance and corresponding GCD curves. **e** Long-cycle performance under 3 A g^{-1} and high loading capacity at 0.5 A g^{-1}.

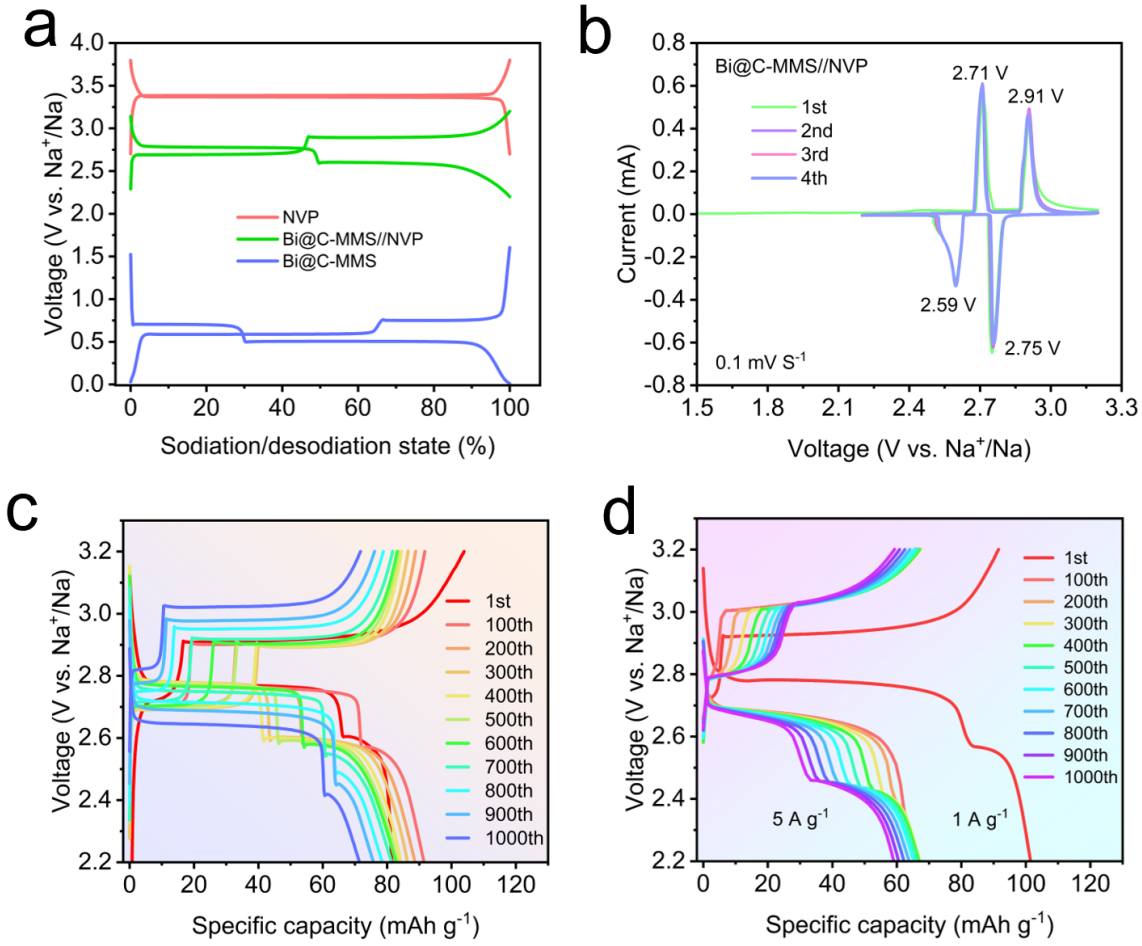

Fig. S29. a Typical GCD curves of NVP cathode, Bi@C-MMS anode, and full cells. **b** CV curves of full cells at 0.1 mV s^{-1}. Long cycling GCD curves for the full cells at current densities of (**c**) 1 A g^{-1} and (d) 5 A g^{-1}.

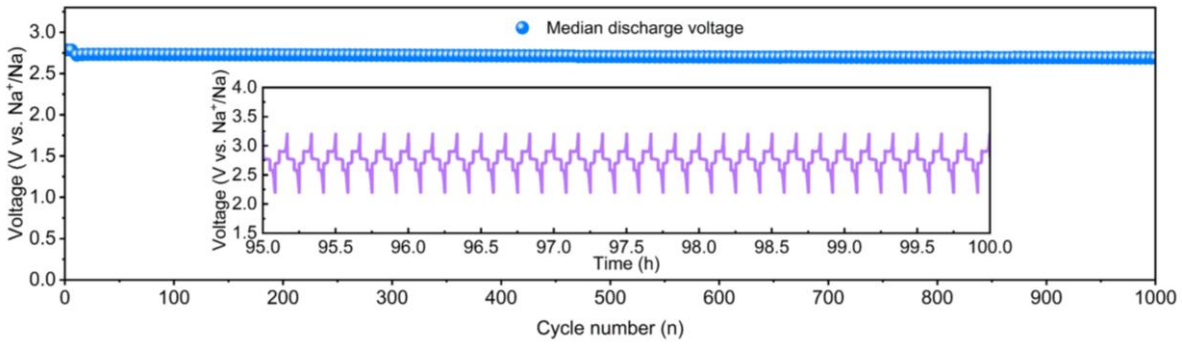

Fig. S30. Median discharge voltage and voltage-time curve of full cells at 1 A g^{-1}.

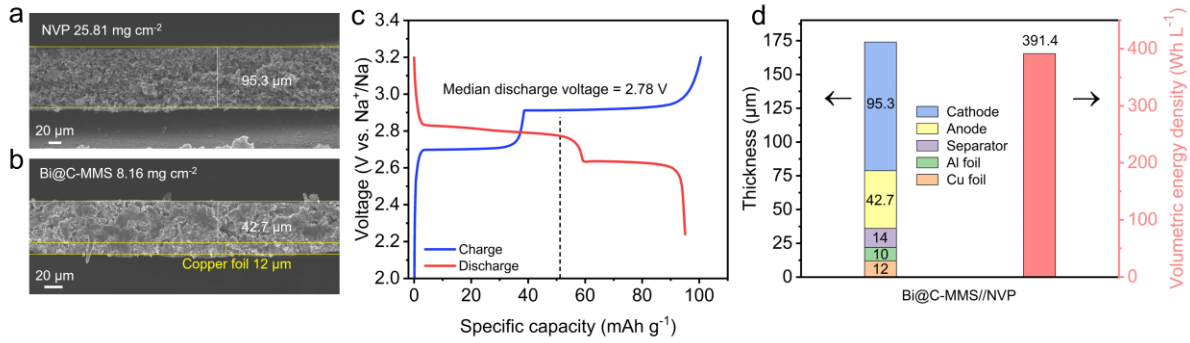

Fig. S31. a, **b** The electrode thickness of a Bi@C-MMS//NVP full cell. **c** GCD curve for the first cycle of the full cell. **d** Calculation of volumetric energy density (VED). The VED was calculated using the following formula:

$$VED\ (Wh\ L^{-1}) = \frac{C_{areal} \times V_{init}}{T_{cell}}$$

where: C_{areal} is the areal capacity of the full cell (mAh cm^{-2}), V_{init} is the initial discharge voltage (V), and T_{cell} is the thickness of the total cell include electrode, separator and current collector. In this work, the C_{areal} is 2.45 mAh cm^{-2} (**Fig. 7e**), initial discharge voltage is 2.78 V, total full cell thickness is 174 μm. Thus, the VED was determined using the equation:

$$VED\ (Wh\ L^{-1}) = \frac{C_{areal} \times V_{init}}{T_{cell}} = \frac{2.45 \times 2.78 \times 10^3}{10^3 \times \frac{174}{10^4}} = 391.4\ Wh\ L^{-1}$$

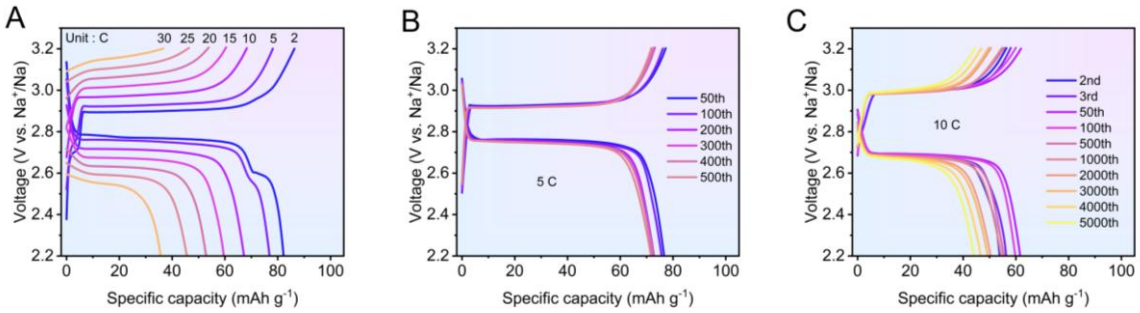

Fig. S32. a GCD curves for the rate performance of pouch cells and long-cycle GCD curves at (**b**) 5 C and (**c**) 10 C.

Tables

Table S1. Comparative electrochemical performance of different anode types in half-cells.

Materials	ICE (%)	Reversible areal capacity (mAh cm^{-2})	Rate capability (A g^{-1})	Active material content (%)	Cycling stability (cycles)	Capacity retention (%)	Ref.
Bi@C-MMS	**90**	**6.7**	**250**	**91**	**14000**	**98.4**	**This work**
nano-Bi@HC	73	5	200	86.2	5000	86	[5]
Bi@C	50.3	3.2	60	52.5	15000	95	[6]
BiNC	95.3	0.398	100	79.7	15000	77.5	[7]
μ-Sn	79.1	3.5	4	80	3000	75.6	[8]
HBiC	79.9	2.66	200	67	15000	90	[9]
CCFSF	80.3	2.19	2.6	20	1000	64	[10]
MGS (LIBs)	93	3.63	0.09	6.3	50	91	[11]
Bi@ Graphite	74.5	0.082	48	30	10000	90	[12]
Bi@C -MS	80	2.8	200	85	12000	85.6	[13]

Table S2. Comparative analysis of the Bi@C-MMS//NVP full cell versus existing SIB full cells.

Anode	Cathode	Current Density ($A\ g^{-1}$)	Cycle number (n)	Capacity retention (%)	Rate capability ($A\ g^{-1}$)	Reference
Bi@C-MMS	**NVP**	**1.0**	**500** **1000**	**93.8** **80.0**	**7**	**This work**
BWC	NVP	0.1	100	54.6	-	[14]
HC	NVP-P-F	0.117	300	80.1	0.585	[15]
Graphite	NNM	0.1	200	74	-	[16]
HC-2	NVP@C	0.02	60	81.9	1	[17]
HC1200-0.5	P2-NLNMOF	0.1	110	85.3	2	[18]
HC	PB	0.17	400	80.57	0.255	[19]
KRN-LA133	NVP	0.08	120	82.9	-	[20]
SP–HC	NVP	1	500	92.0	1	[21]
STHC-MS	NVP	0.117	250	91.7	2.34	[22]
HBiC	NVP	1	100	100	5	[9]

Table S3. Comparative of the Bi@C-MMS//NVP pouch cell versus existing SIB pouch cells.

Anode	Cathode	Current Density ($A\ g^{-1}$)	Cycle number (n)	Capacity retention (%)	Rate capability ($A\ g^{-1}$)	Reference
Bi@C-MMS	**NVP**	**1.0**	**1000** **2000** **5000**	**87.2** **80.5** **70.8**	**3**	**This work**
SLMC	NFM	0.16 1.12	700 500	93.1 92.9	0.96	[23]
JH-1000-30	NFM	0.06	500	81.0	0.6	[24]
BLBWC	NVP	0.1	100	90.2	-	[14]
HC-AA-AIR	PB	0.075	200	73.18	0.3	[25]
KRN-LA133	NFM	0.16	200	80.4	-	[20]
HC	NFM	0.08	1000	90	0.48	[26]
HC	NFM	0.02	100	90	-	[16]
HC	NFM	0.048	800	82.8	-	[27]
HC	NVP	0.585	200	91.7	-	[28]
HC-GI-1605	NVP	0.6	200	90.2	1.5	[29]
Sn/SnO2-CN	NVP/C	1.694	400	76.75	-	[30]

Supplementary movies

Supplementary movies l: Comparison of the sodiation rates for Bi@C-MMS and Bi@C-SP obtained via chemo-mechanical simulation.

Supplementary movies 2-4: In-situ TEM movies documented the morphological evolution of Bi@C-MMS composites in the planar direction during the first three cycles of Na^+ insertion.

Supplementary movies 5, 6: In-situ TEM movies documented the morphological evolution of Bi@C-MMS composites along their thickness during the initial Na^+ insertion process.

Supplementary movies 7, 8: In-situ SEM micro-mechanical testing videos demonstrated the morphological evolution of Bi@C-MMS particles during loading and unloading processes.

Reference

1 Xiao, Q. *et al.* Inward lithium-ion breathing of hierarchically porous silicon anodes. *Nat. Commun.* **6**, 8844 (2015).

2 Yang, H. *et al.* A chemo-mechanical model of lithiation in silicon. *J. Mech. Phys. Solids* **70**, 349-361 (2014).

3 Wang, B. *et al.* Mechanically and chemically Co-robust Ni-rich cathodes with ultrahigh capacity and prolonged cycle Life. *Angew. Chem. Int. Ed.* **64**, e202502725 (2025).

4 Li, Y.-S. *et al.* Mechanically adaptive cathode–electrolyte interphase via dynamic covalent chemistry for long-life Ni-rich lithium batteries. *J. Am. Chem. Soc.* **147**, 36244-36253 (2025).

5 Lu, Z. *et al.* Nano-Bi@hard carbon composite anode for sodium-ion batteries with 385 Wh L^{-1} volumetric energy density and durability. *J. Am. Chem. Soc.* **147**, 28714-28722 (2025).

6 Xiong, P. *et al.* Bismuth nanoparticle@carbon composite anodes for ultralong cycle life and high-rate sodium-ion batteries. *Adv. Mater.* **31**, 1904771 (2019).

7 Long, H. *et al.* Enable the domino-like structural recovering in bismuth anode to achieve fast and durable Na/K storages. *Angew. Chem. Int. Ed.*, e202406513 (2024).

8 Zheng, C. *et al.* Electrostatic shielding boosts electrochemical performance of alloy‐type anode materials of sodium‐ion batteries. *Angew. Chem. Int. Ed.* **62** (2022).

9 Qiu, X. *et al.* Superstructured mesocrystals through multiple inherent molecular interactions for highly reversible sodium ion batteries. *Sci. Adv.* **7**, eabh3482 (2021).

10 Sun, Z.-H. *et al.* Solvent-free ultrafast construction of Se-deficient heterojunctions of bimetallic selenides toward flexible sodium-ion full batteries. *Adv. Mater.* **36**, 2308987 (2024).

11 Ma, J. *et al.* Towards maximized volumetric capacity via pore-coordinated design for large-volume-change lithium-ion battery anodes. *Nat. Commun.* **10**, 475 (2019).

12 Chen, J. *et al.* Intercalation of Bi nanoparticles into graphite results in an ultra-fast and ultra-stable anode material for sodium-ion batteries. *Energy Environ. Sci.* **11**, 1218-1225 (2018).

13 Pan, J. *et al.* Mechanically robust Bismuth-embedded carbon microspheres for ultrafast charging and ultrastable sodium-ion batteries. *J. Am. Chem. Soc.* **147**, 3047-3061 (2025).

14 Jiang, S.-J. *et al.* Lignocellulolytic bacterial engineering for tailoring the microstructure of hard carbon as a sodium-ion battery anode with fast plateau kinetics. *J. Am. Chem. Soc.* **147**, 8088-8092 (2025).

15 Jiang, S. *et al.* Thermodynamically self-limiting presodiation inducing homogeneous inorganic–organic polymer-skeleton interphases for durable sodium-ion batteries. *Adv. Mater.*, e16499 (2025).

16 Wang, X. *et al.* Anion-mediated approach to overcome oxidation in ether electrolytes for high-voltage sodium-ion batteries. *Nat. Commun.* **16**, 2536 (2025).

17 Xue, Y. *et al.* Substitution index-prediction rules for low-potential plateau of hard carbon anodes in sodium-ion batteries. *Adv. Mater.* **37**, 2417886 (2025).

18 Feng, X. *et al.* Critical role of ultra-microporous tunnel structure within hard carbon in boosting sodium-ion storage. *Adv. Mater.*, e01779 (2025).

19 Wan, Y. *et al.* Ion–dipole interactions modulated anion-reinforced solvation chemistry for advanced wide-temperature sodium-ion full batteries. *J. Am. Chem. Soc.* **147**, 29939-29948 (2025).

20 Liu, M. *et al.* Constructing continuously-distributed and crystalline-NaF-rich SEI on hard carbon anode through binder chemistry for high-performance sodium-ion batteries. *Adv. Mater.* **37**, e05368 (2025).

21 Tang, C. *et al.* Bicontinuous structure mediated microstructural engineering of hard carbon for enhanced sodium storage. *Adv. Mater.*, e11632 (2025).

22 Wen, Z. *et al.* Molecular stitching in polysaccharide precursor for fabricating hard carbon with ultra-high plateau capacity of sodium storage. *Adv. Mater.* **37**, 2420251 (2025).

23 Jin, X. *et al.* Solid–liquid metal single-atom clusters for ultrafast kinetics in fast-charging Na-ion batteries. *J. Am. Chem. Soc.* **147**, 33518-33529 (2025).

24 Huang, P. *et al.* Spatiotemporal evolution in hard carbon synthesis via electrothermal coupling strategy for high-performance sodium-ion batteries. *Adv. Mater.* **37**, 2507521 (2025).

25 Chen, Q. *et al.* High-compaction spherical carbon with tunable rich pore structures for efficient sodium storage. *Adv. Mater.*, e15495 (2025).

26 Liao, Y. *et al.* Pentafluoro(phenoxy)cyclotriphosphazene stabilizes electrode/electrolyte interfaces for sodium-ion pouch cells of 145 Wh Kg^{-1}. *Adv. Mater.* **36**, 2312287 (2024).

27 Cui, X. *et al.* 4.2 V O3-layered cathodes in sodium-ion pouch cells enabled by an intermolecular-reinforced ether electrolyte. *Adv. Mater.* **37**, 2415611 (2025).

28 Zhao, J. *et al.* Realizing a 3 C fast-charging practical sodium pouch cell. *Angew. Chem. Int. Ed.* **64**, e202501208 (2025).

29 Ge, Y. *et al.* Insights into the dynamical sodium occupancy evolution and rate-limiting steps in hard carbon. *J. Am. Chem. Soc.* **147**, 39537-39546 (2025).

30 Li, Y. *et al.* In situ-formed C-N anchors embedded into Sn-based negative electrodes for long-life Na-ion batteries. *Nat. Commun.* **17**, 2476 (2026).